IOP Publishing Journal of Physics D: Applied Physics

J. Phys. D: Appl. Phys. **46** (2013) 045002 (13pp) doi:10.1088/0022-3727/46/4/045002

Heat generation in agglomerated ferrite nanoparticles in an alternating magnetic field

E Lima Jr[1], E De Biasi[1,4], M Vasquez Mansilla[1,4], M E Saleta[1], M Granada[1], H E Troiani[1], F B Effenberger[2], L M Rossi[2], H R Rechenberg[3] and R D Zysler[1]

[1] CONICET/Centro Atómico Bariloche, S. C. Bariloche, 8400 Argentina
[2] Instituto de Química, Universidade de Sao Paulo, 05508-000, Brasil
[3] Instituto de Física, Universidade de Sao Paulo, 05508-050, Brasil

E-mail: lima@cab.cnea.gov.ar

Received 6 September 2012, in final form 20 November 2012
Published 20 December 2012
Online at stacks.iop.org/JPhysD/46/045002

Abstract

The role of agglomeration and magnetic interparticle interactions in heat generation of magnetic ferrofluids in an ac magnetic field is still unclear, with apparent discrepancy between the results presented in the literature. In this work, we measured the heat generating capability of agglomerated ferrite nanoparticles in a non-invasive ac magnetic field with $f = 100\,\text{kHz}$ and $H_0 = 13\,\text{kA m}^{-1}$. The nanoparticles were morphologically and magnetically characterized, and the specific absorption rate (SAR) for our ac magnetic field presents a clear dependence on the diameter of the nanoparticles, with a maximum SAR $= 48\,\text{W g}^{-1}$ for 15 nm. Our agglomerated nanoparticles have large hydrodynamic diameters, thus the mechanical relaxation can be neglected as a heat generation mechanism. Therefore, we present a model that simulates the SAR dependence of the agglomerated samples on the diameter of the nanoparticles based on the hysteresis losses that is valid for the non-linear region (with H_0 comparable to the anisotropy field). Our model takes into account the magnetic interactions among the nanoparticles in the agglomerate. For comparison, we also measured the SAR of non-agglomerated nanoparticles in a similar diameter range, in which Néel and Brown relaxations dominate the heat generation.

(Some figures may appear in colour only in the online journal)

1. Introduction

Magnetic fluid hyperthermia (MFH) is a process where the increment of temperature in a target tissue is achieved by the magnetic losses of a ferrofluid constituted by magnetic nanoparticles in a liquid medium in the presence of an ac magnetic field. MFH has been presented as a promising oncology protocol in many *in vitro* and *in vivo* studies [1–5]. The nanoparticles used for MFH, in general, are based on superparamagnetic iron oxide systems, especially magnetite (Fe_3O_4) and maghemite (γ-Fe_2O_3) because of their biocompatibility and high magnetization [6].

The heat generation mechanism in a ferrofluid containing dispersed superparamagnetic nanoparticles in an ac magnetic field is described by two distinct relaxation processes of magnetization. One of these mechanisms is related to the mechanical movement of the particles in the fluid, the so-called Brown relaxation process. The other relaxation process is related to the fluctuation of magnetization through energy barriers and it can be produced in two ways, depending on the temperature, anisotropy of the system and the characteristic relaxation time of the experiment (which in the hyperthermia experiments is given by the frequency of the ac magnetic field). In the superparamagnetic regime, the contribution for heat generation is given by the magnetic losses as a consequence of the delay between the response of the

[4] These authors contributed the same amount to this paper.

magnetization and the ac magnetic field, which is the so-called Néel mechanism. Several works [7–11] have interpreted the specific absorption rate (SAR) measurements of ferrofluids in terms of the Néel and Brown mechanisms, as theoretically treated in Rosensweig's model [12]. However, for blocked systems (relaxation frequency lower than the frequency of the ac applied field), the contribution for heat generation from magnetic losses is given by the internal area of the hysteresis loop, as discussed by Landau and Lifshitz [13] and Usov [14]. When the amplitude of the ac magnetic field amplitude (H_0) is very small in comparison with the energy barrier, the linear approximation assumption is also valid (see [15]). However, when H_0 is significant in comparison with the anisotropy field H_K, the linear approximation is not valid [16].

The heat generating capacity of a ferrofluid is measured by the SAR. Large SAR values lead to high efficiency of MFH, with a lower exposure of the patient to the magnetic material and ac field, reducing the damage in the adjacent healthy tissues [17]. For synthetic ferrite nanoparticles, the highest SAR value observed was about $600\,\mathrm{W\,g^{-1}}$ for iron oxide nanoparticles with $\sim$ 15 nm for a magnetic field with high amplitude and frequency ($H_0 = 12\,\mathrm{kA\,m^{-1}}$ and $f = 400\,\mathrm{kHz}$, respectively) [19], and for $f = 260\,\mathrm{kHz}$ and the same H_0, an SAR value as high as $120\,\mathrm{W\,g^{-1}}$ (bimodal nanoparticles) [7] and $350\,\mathrm{W\,g^{-1}}$ (monodisperse nanoparticles) [20] were observed. Noh *et al* [21] have recently reported SAR values as high as $4000\,\mathrm{W\,g^{-1}}$ for 15 nm core–shell nanoparticles ($MnFe_2O_4$@$CoFe_2O_4$) and $10\,600\,\mathrm{W\,g^{-1}}$ for 60 nm core–shell cubic nanoparticles ($Zn_{0.4}Fe_{2.6}O_4$@$CoFe_2O_4$) for an ac magnetic field of $f = 500\,\mathrm{kHz}$ and $H_0 \sim 35\,\mathrm{kA\,m^{-1}}$ via control of the surface and exchange anisotropy in order to optimize the ferrimagnetic hysteresis.

Magnetic and morphological characteristics of the nanoparticles (anisotropy, magnetization, shape and size) are not the only parameters that determine the SAR. Agglomeration and concentration of the nanoparticles are also important factors to be taken into account for the optimization of the SAR and crucial for the application of nanoparticles in hyperthermia clinical protocols. Eggeman *et al* [22] studied the effects of nanoparticle agglomeration on high-frequency hysteresis, showing that highly clustered samples can be heated within an ac magnetic field, while a fully dispersed sample showed no measurable heating. In another way, Urtizberea *et al* [23] found that the SAR of a ferrofluid containing non-agglomerated and crystalline maghemite nanoparticles with 11.6 is doubled when the concentration of the nanoparticles decreases by a factor of 4, as a consequence of the interparticle interactions. This result indicates that agglomeration and interparticle interaction are also apparently key parameters in order to optimize the SAR of a nanoparticle-based ferrofluid. However, Jeun *et al* [24] found that $MgFe_2O_4$ and $NiFe_2O_4$ agglomerate nanoparticles present significant SAR, and for their systems the agglomeration promotes an increment of the heat generated by an ac magnetic field in the kilohertz frequency range. Similar results were observed for *in vivo* tests of Fe_3O_4 nanoparticles, in the kHz range too, by Dennis *et al* [25], observing a *quasi*-total regression of mammary tumour in mice. Therefore, these apparently discrepant results reveal that the role of agglomeration and magnetic interparticle interactions in the heat generation of magnetic ferrofluids is still unclear.

An interesting system to investigate the effects of interparticle interactions on the heat generation of nanoparticles is the magnetosome. Magnetosomes are magnetite crystals produced by a biomineralization process in magnetotactic bacteria. Hergt *et al* [18] measured a SAR as high as $960\,\mathrm{W\,g^{-1}}$ for magnetosomes of $d = 15\,\mathrm{nm}$ at a field of 410 kHz and $10\,\mathrm{kA\,m^{-1}}$, while Timko *et al* [26] found SAR $= 171\,\mathrm{W\,g^{-1}}$ for $5\,\mathrm{kA\,m^{-1}}$ and 750 kHz. In both works, the magnetosomes are composed of interacting nanoparticles forming chain-like structures. Hergt *et al* [27] theoretically dealt with the hysteresis losses observed for magnetosomes with a phenomenological model, where an empirical expression for the dependence of hysteresis is used by assuming a monodisperse system. According to the authors, the Stoner–Wolfarth model cannot explain the experimental measurements for magnetosomes. These results evidence the necessity of a better theoretical treatment of the problem, taking into account the interparticle interactions.

In this work, we measured the heat generating capability of agglomerated ferrite nanoparticles (hydrodynamic diameter $d_{\mathrm{hyd}} > 200\,\mathrm{nm}$, where the particle rotation mechanism for heat generation is not important) for a non-invasive ac magnetic field with $f = 100\,\mathrm{kHz}$ and $H_0 = 13\,\mathrm{kA\,m^{-1}}$. The nanoparticles were morphologically and magnetically characterized, and the SAR presents a clear dependence on the diameter of the nanoparticles, with a maximum SAR $= 48\,\mathrm{W\,g^{-1}}$ at 15 nm. We also present a model to determine the SAR dependence on the diameter of the nanoparticles based on the hysteresis losses that is valid for the non-linear region (with H_0 comparable to the anisotropy field). Our model takes into account the magnetic interactions among the agglomerate nanoparticles. Finally, the dependence of the SAR of agglomerated and interacting nanoparticles is simulated, and for comparison, we also measured the SAR of non-agglomerated nanoparticles in a similar diameter range. In this way, our result could be of great interest in order to understand the mechanism behind the heating mechanism of agglomerated nanoparticles and consequently for future applications in MFH clinical protocols.

2. Experimental details

2.1. Sample preparation

Two sets of samples composed of ferrite nanoparticles were synthesized by high-temperature decomposition of Fe(III) acetylacetonate ($Fe(acac)_3$) in the presence of a long-chain alcohol and surfactants (oleic acid and oleylamine) using phenyl ether (boiling point $\sim$533 K) as the solvent. The first set consists of samples with a distinct diameter prepared by a successive synthesis procedure using smaller nanoparticles as seeds. The first sample of this set, labelled A01, was synthesized as reported elsewhere [25], using 2 mmol of $Fe(acac)_3$, 4 mmol of oleylamine, 6 mmol of oleic acid, 10 mmol of 1,2-octanediol and 20 ml of phenyl ether under

vigorous magnetic stirring and flow of N_2. The final mixture was heated at 483 K and then refluxed for 120 min in N_2 atmosphere. One part of this solution was kept as seeds for the synthesis of the next sample, and the other part was treated with ethanol in order to precipitate the iron oxide nanoparticles, which were separated through centrifugation (7000 rpm/30 min). Centrifugation and the washing procedure with ethanol and dichloromethane were repeated three times. The final particle size of sample A01 is 5.5 nm and $\sigma = 0.2$, as reported elsewhere [28]. Other samples were produced by subsequent seed growth processes and using the previously synthesized nanoparticles as seeds (in an over-saturated solution). In a typical preparation, 10 ml of the previously synthesized nanoparticle solution (for instance, A01) were added to a mixture similar to that described above. The final mixture was heated at 483 K and refluxed for 120 min in N_2 atmosphere. One part of this solution was kept for the next growth process, and the iron oxide nanoparticles in the other part of the solution were precipitated by adding ethanol and through centrifugation with a relative centrifugation force RCF = 5862 g (7000 rpm in our equipment) for 30 min several times. These samples produced by the subsequent growth processes were labelled AYY, where YY indicates the number of times the re-crystallization has taken place, starting with sample A01 composed of 5.5 nm nanoparticles followed by samples A02, A03, A04 and A05. The re-crystallization time is added for each sample: the total crystallization time increases from 120 min for sample A01 to 600 min for A05. The excessive crystallization time and the exhaustive washing procedure lead to agglomeration of the nanoparticles in samples A02–A05, and the agglomeration of nanoparticles used as seeds may lead to a non-continuous increase in the diameter of the nanoparticles after each re-crystallization procedure.

The second set of samples consists of non-agglomerated nanoparticles (dispersed samples), which were synthesized by the thermal decomposition of $Fe(acac)_3$ at high temperatures and without the use of seeds, based on the method described in [29]. The final size of the nanoparticles was controlled by the relation [precursor] : [surfactant] [30]. Seven samples with different mean diameters were synthesized in this set, labelled DXX, where XX indicates the mean diameter of the nanoparticles. More details concerning the synthesis of the dispersed samples can be found in [31, 32].

2.2. Experimental techniques

Transmission electron microscopy (TEM) images of the nanoparticles were obtained in a PHILIPS-CM200 microscope operated at 200 kV and the TEM specimens were prepared by dropping a suspension with low concentration of the particles over a thin carbon-covered copper grid. The x-ray patterns were taken in a Philips PW 346 diffractometer using the Cu K_α radiation ($\lambda = 0.154\,186$ nm) at room temperature with the sample conditioned over a glass surface.

Magnetization measurements as a function of temperature ($M(T)$) and magnetic field ($M(H)$) were performed in a LakeShore vibrating sample magnetometer (VSM). $M(T)$ curves were measured under zero-field-cooling ($M_{ZFC}(T)$) and field-cooling ($M_{FC}(T)$) conditions with an applied field of 4 kA m^{-1} and in the temperature range 83 K $< T <$ 300 K or 5 K $< T <$ 300 K, depending on the sample. $M(H)$ measurements were performed at 300 K within the applied field range $-800\,\text{kA m}^{-1} \leqslant H \leqslant 800\,\text{kA m}^{-1}$. For all magnetic measurements, the nanoparticles were fixed in a polymeric matrix (polyethylenimine—PEI) at a concentration lower than 1% wt.

Hydrodynamic diameters were measured by light dispersion in a ZetaSizer 1000, Malvern Instruments, with the nanoparticles dispersed in toluene at very low concentrations. Each sample was measured between 5–10 times to improve the statistics.

We measured the SAR in a homemade ac magnetic field generator using an LC resonant circuit. The field was generated by a copper coil, refrigerated with water, wrapped in a core of ferrite (green type) with a gap of 3 cm where the sample is positioned. The field has frequency $f = 100$ kHz and amplitude $H_0 = 13\,\text{kA m}^{-1}$. The amplitude of the applied field varies about 5% inside the gap. The nanoparticle-based ferrofluid (nanoparticles dispersed in toluene with concentration of 1 wt%) is taken in a glass vessel with double wall vacuum isolated in a quasi-adiabatic configuration, leading to an underestimation of about 15% of the measured SAR values by irradiation [33]. The ferrofluid was sonicated for 30 min before the experiment of duration ~3 min. The temperature was measured with an ethanol thermometer submerged in the ferrofluid and the temperature was recorded at regular time intervals. The thermometer was recorded during the experiment; using this arrangement to measure the temperature, we observe a 10% dispersion of SAR values for different measurements on the same sample. For instance, this dispersion is smaller than that observed for a non-contacting infrared thermometer.

3. Results

In this work, we focused on the heating capability and the heating mechanism for agglomerated nanoparticles in an ac magnetic field. Thus, our results are centred on samples A01–A05. Magnetic and morphological characterizations of nanoparticles similar to the dispersed samples are given in [34, 35].

Figures 1(*a*)–(*e*) present the TEM images of the agglomerated samples A01–A05. The insets show the respective histograms, which were fitted with a lognormal distribution for samples A01–A05. The values of the most probable diameter (d_{TEM}) and dispersion (σ) obtained from the fitting are given in table 1. It is important to note that these images are not completely representative of the system, since several agglomerates were observed for different zones of the nanoparticles. We select these images (with more dispersed nanoparticles) due to the clarity in observing the isolated nanoparticles. The histograms were constructed by measuring the diameter of the nanoparticles of several regions, including agglomerates.

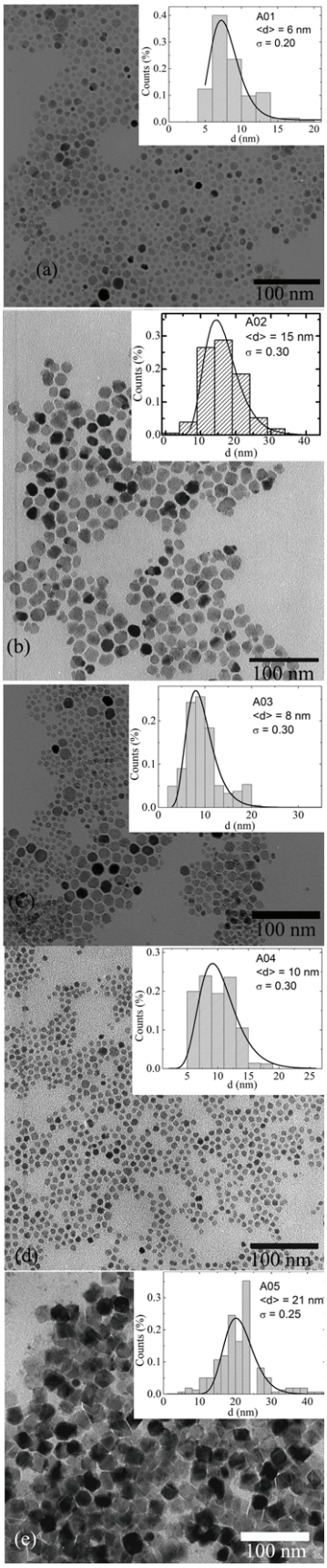

Figure 1. TEM images of samples A01–A05 (*a*)–(*e*, respectively). The insets show the size histograms obtained from the respective TEM images fitted with lognormal curves (solid lines).

Interestingly, the diameter of the nanoparticles does not increase after each re-crystallization process, possibly as a consequence of the polydispersion and agglomeration of the seeds, in addition to the Ostwald ripening [36].

Figures 2(*a*) and (*b*) show high-resolution TEM images (HRTEM) of samples A01 and A05 as representative of the systems. From this analysis, the nanoparticles present high crystallinity and the fast Fourier transform (FFT) of the HRTEM images is consistent with (for instance, see the top panel of each image) the spinel structure expected for ferrite, which is confirmed by the x-ray diffraction (XRD) analysis (figure 3).

Morphological (TEM and XRD) and magnetic characterizations of DXX samples (dispersed nanoparticles) are presented elsewhere [31, 32]. As a representative of these systems, figure 4 displays the TEM image of samples D08 (figure 4(*a*)) and D18 (figure 4(*b*)). The insets give the respective diameter histograms fitted with a lognormal distribution. The mean diameter $\langle d \rangle$ and the size dispersion σ obtained from the TEM analysis of all the dispersed samples are given in table 1. High-resolution TEM (HRTEM) and XRD analyses of the dispersed samples confirm that the nanoparticles are crystalline with the spinel structure of ferrites.

The $M_{\mathrm{ZFC}}(T)$ and $M_{\mathrm{FC}}(T)$ curves of AYY are presented in figures 5(*a*)–(*e*), and except for samples A01 the curves reflect the absence of the superparamagnetic (SPM) regime for agglomerated samples in the range $T < 300$ K in the dc measurements. Therefore, these systems are not in the SPM regime for dc conditions and are definitely not in the SPM regime in the SAR experiment ($f = 100$ kHz) and the principal contribution to heat generation is the hysteresis losses. Some $M_{\mathrm{ZFC}}(T)$ and $M_{\mathrm{FC}}(T)$ curves are untypical, reflecting the interparticle interaction. In addition, these curves do not attain the irreversibility temperature, especially in figure 5(*e*), where the experiment did not allow enough time for the relaxation of the system. The important feature of these curves is to give evidence of the interparticle interactions in the agglomerated samples, as well as to show the high blocking temperature of these systems. The $M_{\mathrm{ZFC}}(T)$ curves of dispersed samples (DXX) clearly present a maximum at T_{max} (given in table 1) associated with the blocking temperature of the system. The $M(T)$ curves of samples D08 and D18 are given in figures 5(*f*) and (*g*) as a representative of the dispersed systems. The energy barrier distribution estimated from the $M_{\mathrm{ZFC}}(T)$ and $M_{\mathrm{FC}}(T)$ curves of samples DXX is obtained from the plot $(1/T)\mathrm{d}(M_{\mathrm{ZFC}} - M_{\mathrm{FC}})/\mathrm{d}T$ versus T (see the inset of figures 5(*f*) and (*g*)), where the maximum in the curve corresponds to the mean blocking temperature T_{B} of the system and the values obtained vary from 20 K up to 270 K. By extrapolating these values of dc measurements to the frequency of the SAR measurements ($f = 100$ kHz) and using the Néel model, we calculated that T_{B} at 100 kHz (T_{B}^{100}) varies from 55 to 267 K for $\langle d \rangle < 18$ nm and $T_{\mathrm{B}}^{100} = 439$ K for D18 and is larger than 700 K for D23. Thus, at the frequency of the SAR measurements, the systems are in the superparamagnetic regime (SPM), except samples D18 and D23, which are unequivocally in the blocked regime.

Probably, the differences in the $M(T)$ curves between agglomerated and dispersed samples result from the

Table 1. Characterization of samples AYY and DXX: d_{TEM} is the most probable diameter, and σ is the dispersion obtained from the lognormal fit of the size distribution histogram; T_{Max} is the temperature of the maximum in the $(1/T)d(M_{ZFC}(T) - M_{FC}(T))/dT$ curves measured under dc conditions; T_B^{100} is the blocking temperature calculated from T_{max} with the Néel model for $f = 100$ kHz; M_S is the saturation magnetization; $\chi_{13\,kA\,m^{-1}}$ is the susceptibility at $H = 13\,kA\,m^{-1}$ obtained from $M(H)$ curves measured at 300 K and SAR is the specific absorption rate obtained from the T versus t curve of hyperthermia experiments.

Sample	d_{TEM} (nm)	σ	T_{MAX} (K)	T_B^{100} (K)	M_S (kA m^{-1})	$\chi_{13\,kA\,m^{-1}}$ (300 K)	SAR[a] (W g^{-1})
A01	6	0.20	23	60	375	1.75	22
A02	15	0.30	>300	>300	402	1.53	48
A03	8	0.30	>300	>300	365	1.13	15
A04	10	0.30	>300	>300	417	1.51	30
A05	21	0.25	>300	>300	413	2.01	5
D06	6	0.25	20	55	318	1.28	8
D08	8	0.22	30	82	330	1.25	19
D11	11	0.25	65	178	400	1.63	56
D13	13	0.21	82	225	402	1.72	67
D16	14	0.20	97	267	422	1.88	85
D18	18	0.18	160	439	433	2.01	100
D23	23	0.20	270	>700	437	2.26	60

[a] The variance of the SAR value at different measurements of the same sample is 10%.

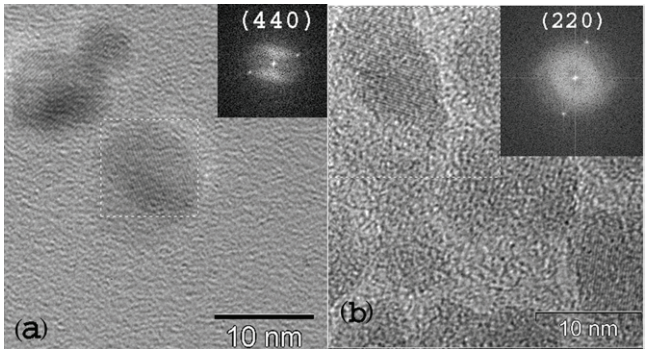

Figure 2. HRTEM images of samples A01 (*a*) and A05 (*b*) as a representative of the systems. Top panel: FFT of the particles indexed according to the crystallographic planes of the spinel structure expected for ferrite.

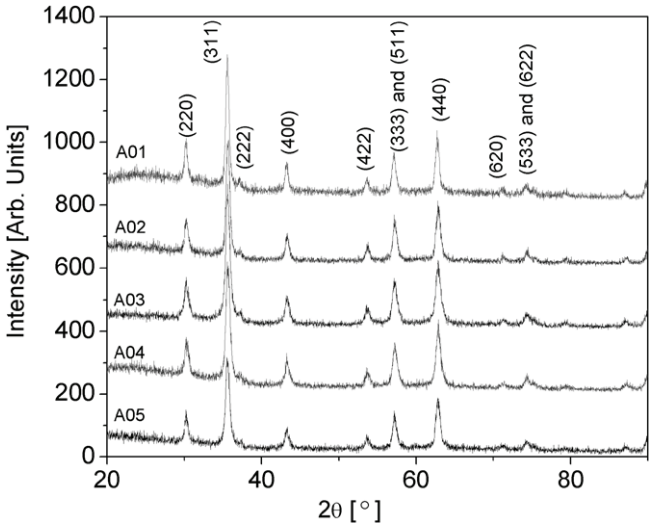

Figure 3. XRD patterns of agglomerated samples (AYY).

stronger interparticle interactions as a consequence of the agglomeration of the nanoparticles, which lead to an increment in the energy barrier and an increase in T_B [35]. In fact, the $M_{FC}(T)$ curves of the agglomerated samples are indicative of the interparticle interactions at low temperatures in comparison with the curves of dispersed samples.

The $M(H)$ curves of samples A01–A05 measured at $T = 300$ K are shown in figure 6. Only sample A05 presents a small coercivity at room temperature (about 6 kA m^{-1}). The other samples present a very small coercive field. The values of M_S are about 400 kA m^{-1} for all samples and the susceptibility values at $H = H_0$ are obtained by differentiation of the $M(H)$ curves (see table 1). The $M(H)$ curves of the dispersed samples do not present coercivity and the values of M_S and $\chi_{13\,kA\,m^{-1}}$ are also given in table 1.

Hydrodynamic diameter measurements also indicate that nanoparticles in samples A02–A05 are agglomerated. For sample A01, we observe a hydrodynamic radius of about 10–15 nm, as expected for dispersed nanoparticles covered with a single layer of oleic acid. In another way, samples A02–A05 present hydrodynamic mean diameters of 230 nm (±30 nm), 202 nm (±30 nm), 260 nm (±50 nm) and 420 nm (±50 nm), respectively, where the number in parentheses refers to the dispersion of the mean hydrodynamic diameter for 10 runs. These results confirm the formation of agglomerates in these samples.

The Brown relaxation time is given by

$$\tau_B = \frac{4\pi\eta(r_{hyd})^3}{k_B T}, \qquad (1)$$

where η is the viscosity of the fluid, k_B is the Boltzmann constant, T is the temperature and r_{hyd} is the hydrodynamic radius. According to equation (1), the Brown relaxation time for our systems A02–A05 is very big in comparison with the ac magnetic field frequency $f = 100$ kHz. In this way, the large hydrodynamic diameters of samples A02–A05 make the Brown contribution to the SAR negligible.

The hydrodynamic diameter of samples DXX varies from 20 to 30 nm, confirming that the nanoparticles in these samples are dispersed. In these cases, the Brown relaxation should be

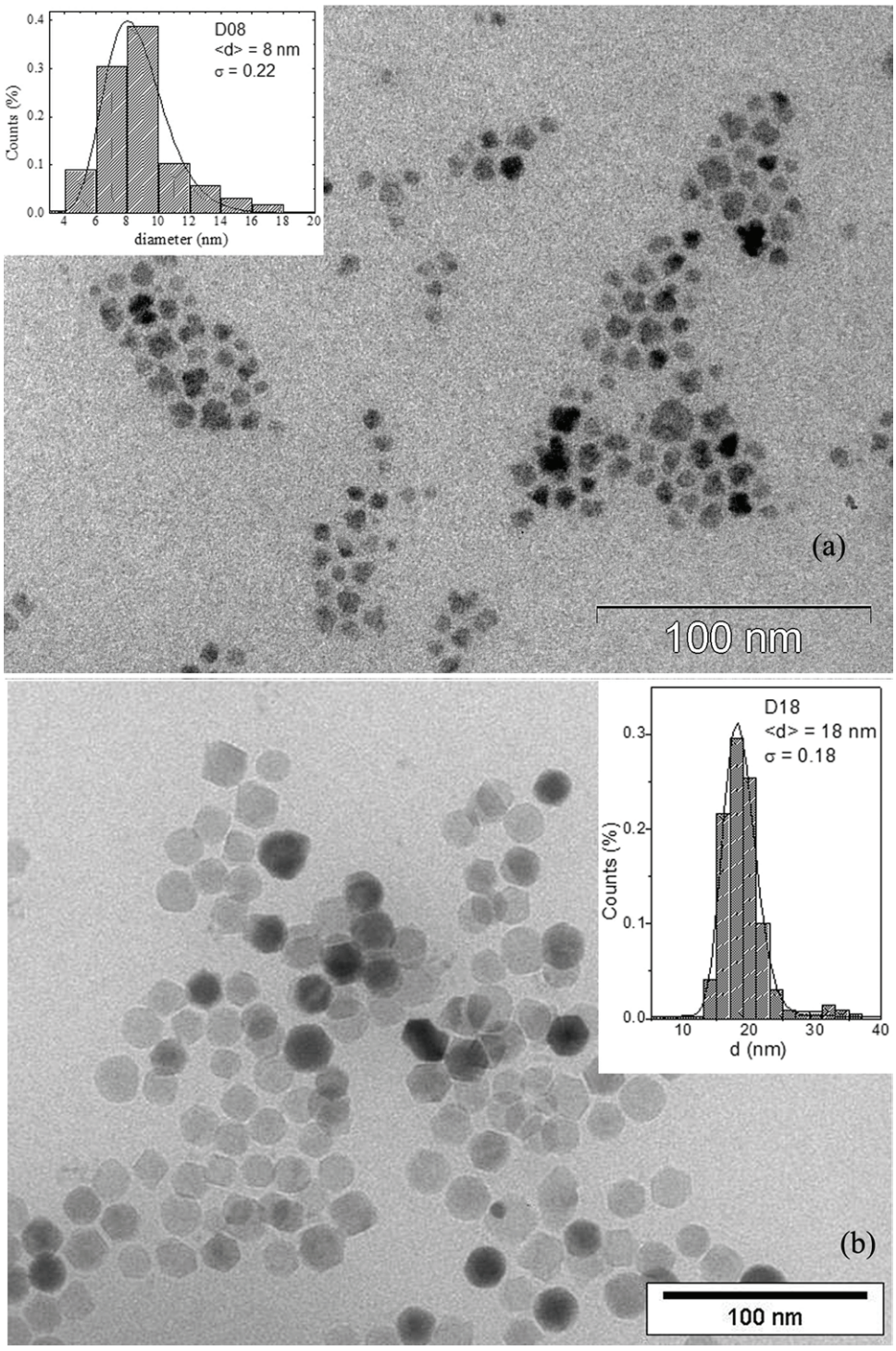

Figure 4. TEM images of samples D08 (*a*) and D18 (*b*) as a representative of the dispersed samples. The insets display the respective diameter histogram fitted with a lognormal distribution (solid line).

considered in heat generation, even for samples D18 and D23, which are in the blocked regime for $f = 100\,\text{kHz}$.

The SAR is defined as the variation of the temperature with time ($\Delta T/\Delta t$) of the ferrofluid in the *ac* magnetic field:

$$\text{SAR} = c\frac{m_{\text{NPs}}}{m_L}\left(\frac{\Delta T}{\Delta t}\right), \tag{2}$$

where c is the specific heat of the fluid per mass unit and m_{NPs}/m_L is the nanoparticle concentration in the fluid. The SAR has units of power per mass of nanoparticles (W g^{-1}). Figure 7(*a*) presents the time dependence of the temperature of agglomerated samples in toluene at 1 wt% concentration after 15 min in ultrasound, and figure 7(*b*) shows the SAR values obtained from these measurements for the agglomerated samples as a function of $\langle d\rangle$, (as obtained from the TEM analysis). These curves show a clear maximum of SAR $=$ $48\,\text{W g}^{-1}$ for sample A02: $\langle d\rangle_{\text{TEM}} = 15\,\text{nm}$. It is interesting to compare the behaviour of samples A01 and A03. According

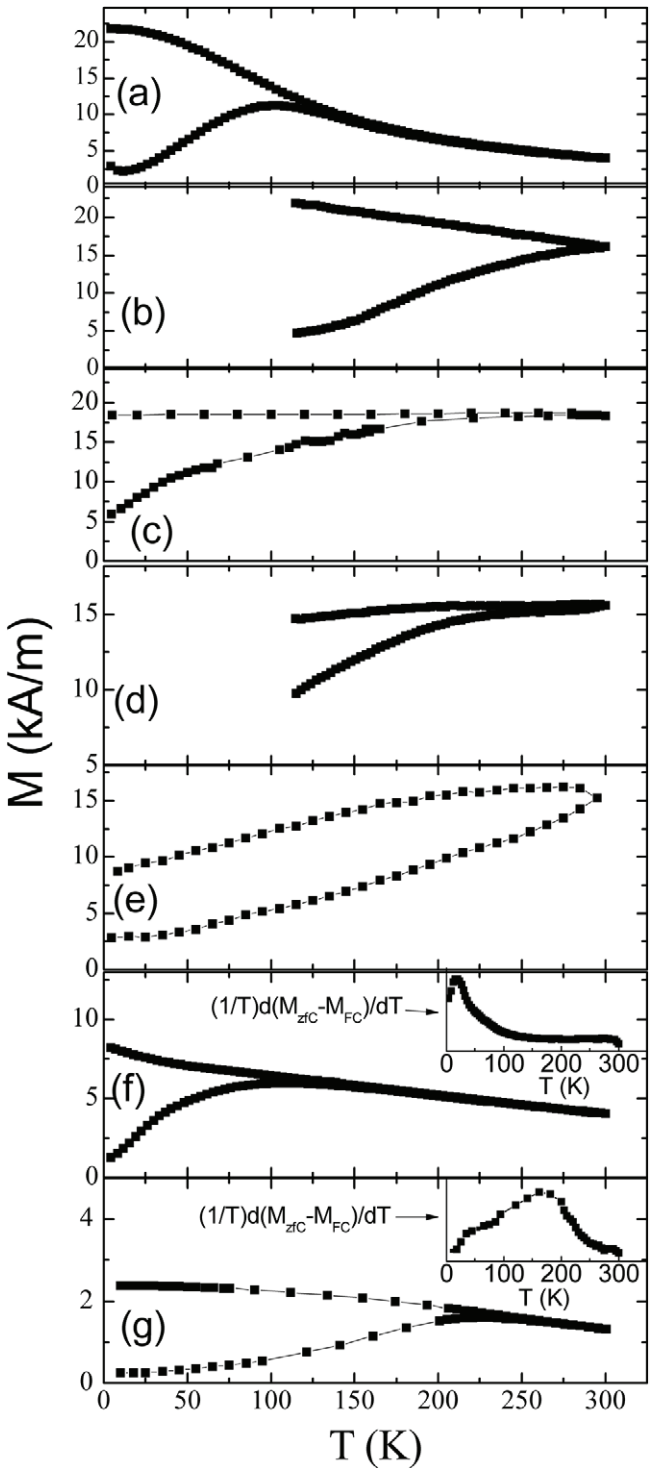

Figure 5. (*a*)–(*e*) $M_{ZFC}(T)$ and $M_{FC}(T)$ curves ($H = 4\,\mathrm{kA\,m^{-1}}$) of AYY samples (agglomerated), and (*f*) and (*g*) for samples D08 and D18, respectively.

to table 1 both nanoparticles have similar $\langle d \rangle$, as well as identical morphology, but the particles of sample A01 are not agglomerated, as indicated by the hydrodynamic radius measurements and magnetic characterization. Then, the fundamental difference between both samples is due to the interparticle interactions. This is a complex topic because interparticle interactions are strongly dependent on the particle size distribution as well as the particular characteristics of the particle arrangement. In figure 7(*b*) we also present the SAR values of the dispersed samples as a function of $\langle d \rangle$, which also exhibits a maximum at $\langle d \rangle = 18\,\mathrm{nm}$.

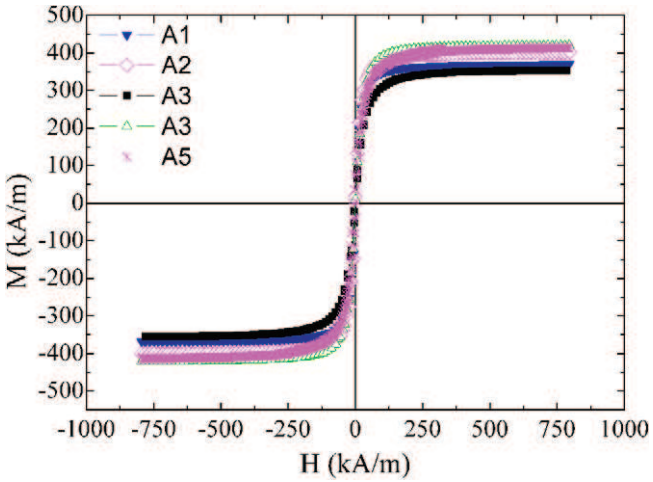

Figure 6. $M(H)$ curves of samples A01–A05 measured at room temperature.

Theory and simulations. In order to take into account the hysteresis losses in the SAR of our interacting nanoparticle systems (samples A02–A05), we propose a model to describe the hysteresis cycle for the time window of our interacting system. The idea of this model is presented in [36] and similar treatments were developed by other authors [38, 39].

The magnetic energy of the non-interacting nanoparticle system can be written as

$$E = \vec{\mu} \cdot \vec{H} - kV(\hat{n} \cdot \hat{\mu})^2, \tag{3}$$

where the first term corresponds to the Zeeman energy and the second one to the magnetic anisotropy. In equation (3), μ represents the magnetic moment, H is the external applied field, K is the magnetic anisotropy constant, V is the volume of the particle and n indicates the easy axis orientation. In this model, we assume uniaxial magnetic anisotropy. Equation (3) gives information about the energy surface at zero temperature. For $KV > \mu \cdot H$, the system presents two minimum states, labelled 0 and 1. Starting from the master equation, it is possible to obtain the temporal evolution of the population at minimum 0 (P^0):

$$P^0_{t+\Delta t} = P^0_t + (P^0_\infty - P^0_t)L, \tag{4}$$

where P^0_∞ represents the equilibrium population ($t \to \infty$), P^0_t is the population at time t, Δt is the experimental temporal window and $L = 1 - \exp[-t/\tau^*]$ is defined as the probability of finding the particle in the superparamagnetic regime, and $\delta\tau*$ is the effective time to pass from a minimum position to the other one. The calculation of each relaxation time is performed using the Arrhenius law: $\tau = \tau_0 \exp(\Delta E \cdot \beta)$, where τ_0 is the characteristic relaxation time, ΔE is the energy barrier and $\beta = 1/k_B T$ is the thermal energy. P^0_∞ is calculated numerically (together with the partition function Z) within each minimum region of the energy surface and using

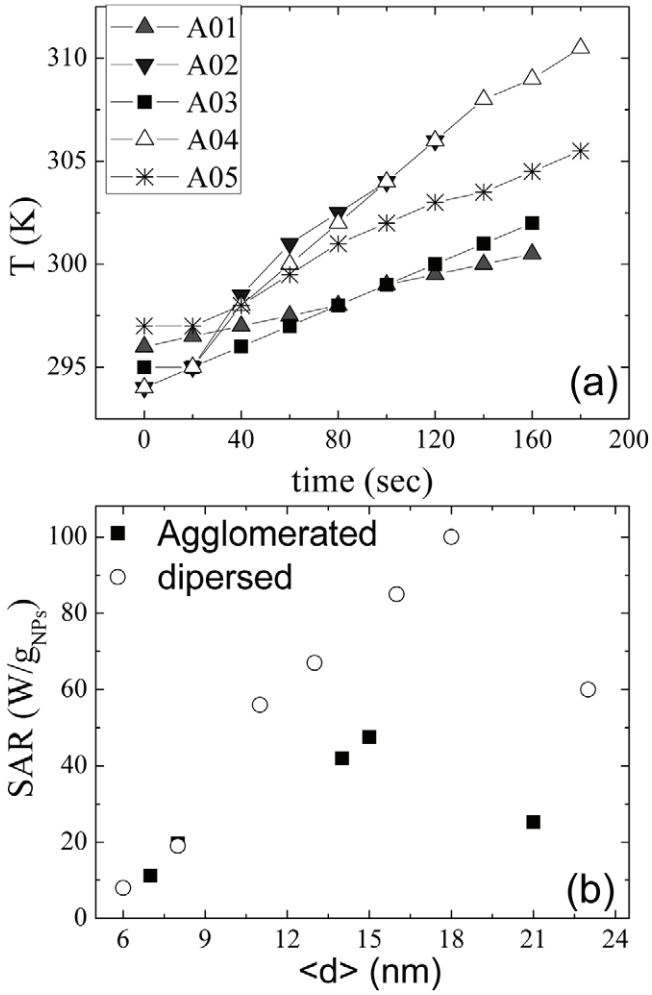

Figure 7. (*a*) Time dependence of the temperature for samples A01–A05 diluted in toluene (1 wt%) in an alternating magnetic field with $f = 100\,\mathrm{kHz}$ and $H_0 = 13\,\mathrm{kA\,m^{-1}}$. (*b*) SAR values for samples A01–A05 and DXX obtained from hyperthermia experiments data using equation (2) as a function of the most probable diameter obtained from TEM analysis.

equation (4), we calculate the temporal evolution of P^0 from the initial value P_t^0.

According to our previous definitions, $L \to 0$ for $T \to 0$ and $L \to 1$ for $T \to \infty$. Thus, we consider superparamagnetic and blocked contributions in separate ways by working with the probabilities L and 1-L, respectively. For the superparamagnetic case, the thermal average is performed by calculating

$$\langle M\rangle_{\mathrm{SP}} = \iint_{\Omega_{\mathrm{Tot}}} f(E,T)(\vec{M}\cdot\vec{H}/H)\,\mathrm{d}\Omega \qquad (5)$$

over all directions on the (θ,φ) space. Here, $f(E,T)$ is the normalized Boltzmann distribution. On the other hand, the blocked case must be treated carefully. We find the minima (θ_i,φ_i) and calculate the average magnetization and anisotropy in the surrounding (θ,φ) values corresponding to each minimum (Ω_i):

$$\langle M\rangle_B^i = \iint_{\Omega_i} f(E,T)(\vec{M}^i\cdot\vec{H}/H)\,\mathrm{d}\Omega. \qquad (6)$$

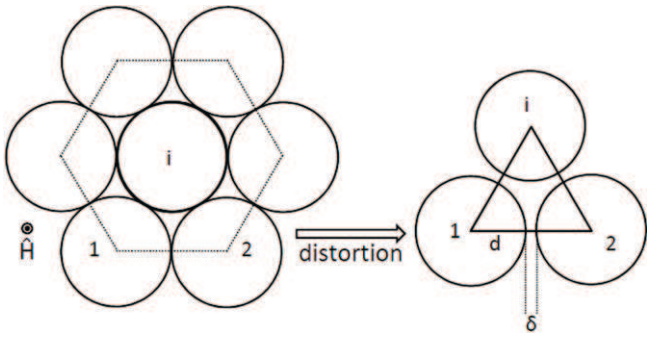

Figure 8. Schematic representation of the relative distortion in the arrangement of the agglomerated nanoparticles.

Finally, the total quantity (magnetization or anisotropy) should be expressed as

$$\langle M\rangle = (1-L)(P_t^0\langle M\rangle_B^0 + P_t^1\langle M\rangle_B^1) + L\langle M\rangle_{\mathrm{SP}}. \qquad (7)$$

Equation (7) gives the evolution of the magnetization as a function of the field, temperature, time window and the previous magnetic history of the system. However, this description involves a non-interacting nanoparticle system. In order to consider the interparticle dipolar interactions, we need to correct equations (6) and (7) by modifying the magnetic field, assuming an effective value using mean field approximation. The reason for the presence of an effective magnetic field can be associated mainly with the inhomogeneities in the particle arrangement. We assume a hexagonal close packed (hcp) arrangement for simplicity, but any other close packed structure could be considered. The hcp arrangement, as well as a cubic face-centred one, is a natural possibility as a consequence of the agglomeration and the spherical shape of the particles.

Usually, the size distribution is important in the case of small particles located close to big ones [40]. In this case, the effect is stronger in the smaller particles by influence of the larger ones. In our case, we are interested in studying the behaviour of the larger particles, because they will provide the main contribution to the hysteresis of the magnetization as a function of the external field (if the magnitude of the external field is close to the anisotropy one). We calculate the mean field interaction for a particle i located at the centre of the hcp structure considering the volume of the 12 nearest neighbours: 6 at the plane forming a hexagonal arrangement and 6 others forming two triangles above and below particle i. The structure considered for interparticle mean field is shown in figure 8. The magnetostatic calculation is made in the dipolar approximation, where the magnetic energy of particle i is given by

$$E_i = \sum_j \left(\frac{\vec{\mu}_i\cdot\vec{\mu}_j}{r_{ij}^2} - 3\frac{(\hat{r}_{ij}\vec{\mu}_j)(\hat{r}_{ij}\vec{\mu}_i)}{r_{ij}^3} \right). \qquad (8)$$

E_i is null for a perfect arrangement, i.e. a structure with no distortion.

However, a distorted arrangement can be easily supported in a real system. For example, the size distribution can be

important to produce a distorted arrangement of particles (see [41]). In this way, the introduction of a distorted arrangement of the nanoparticles in our model is justified. In addition, the magnetic field breaks the spatial symmetry and if the particles are agglomerated in the field direction the magnetic energy is reduced. It is also expected that the magnetic gradient in the H direction leads to the creation of chain-like structures in the particle agglomerate, generating a local effective field. These two effects lead to a distortion of the structure, increasing with δ the distance between particles in the plane perpendicular to the field direction, as shown in figure 8. We assume a distortion of 10% ($\delta/d = 0.1$). With these assumptions, we calculate the effective magnetic field on particle i as

$$\mu_0 H_{\text{eff}} = \mu_0 \left[H + \pi \frac{\langle M \rangle}{d^3} \left(\frac{\delta}{d} \right) \right], \tag{9}$$

where μ_0 is the vacuum magnetic permeability. In this expression, $\langle M \rangle$ is the thermally corrected magnetization of the particle (given by equation (7)).

Numerical calculations of hysteresis loops were made by replacing H in equation (3) by the effective value obtained from equation (9). We consider a variation time of 10^{-5} s between $-H_0$ and H_0 (a frequency of 100 kHz equivalent to the one used in our SAR measurements). We also remark that, in the numerical calculation of the hysteresis cycles, we start by the initial curve of the system (the virgin curve), assuming $P_0^0 = 1/2$ for $H = 0$ (when the dipolar correction is null). In order to make the calculations more realistic we also consider the random angular distribution of the easy axis and the size particle distribution, which is considered to be similar to that obtained from the TEM analysis of our experimental systems.

Figure 9(a) presents the numerically calculated minor loops (up to $H = 13\,\text{kA m}^{-1}$ at 100 kHz) of a nanoparticle system with random easy axis distribution, $K_{\text{eff}} = 3 \times 10^4\,\text{J m}^{-3}$, $\tau_0 = 10^{-11}$ s, $M_S = 500\,\text{kA m}^{-1}$, and $\langle d \rangle = 14$ nm with lognormal distribution ($\sigma = 0.20$). The SAR value due to the hysteresis losses is calculated as the product of the frequency times the loop area. The diameter dependence of the SAR of the interacting systems, calculated from the minor loops up to $13\,\text{kA m}^{-1}$, is given in figure 9(b) and it exhibits a clear maximum between 12 and 14 nm for both curves. In order to compare the SAR values calculated by considering hysteresis losses with the experimental one, we have also plotted the experimental SAR values of samples A01–A05 as a function of $\langle d \rangle$. Discrepancies between theoretical and experimental values may be a consequence of the wider diameter distribution of samples A01–A05 than the one used in our simulation and/or differences in the mean distance and space arrangement of the nanoparticles in our samples, which changes the interparticle interaction strength. However, the theoretical curves and experimental values present similar tendencies.

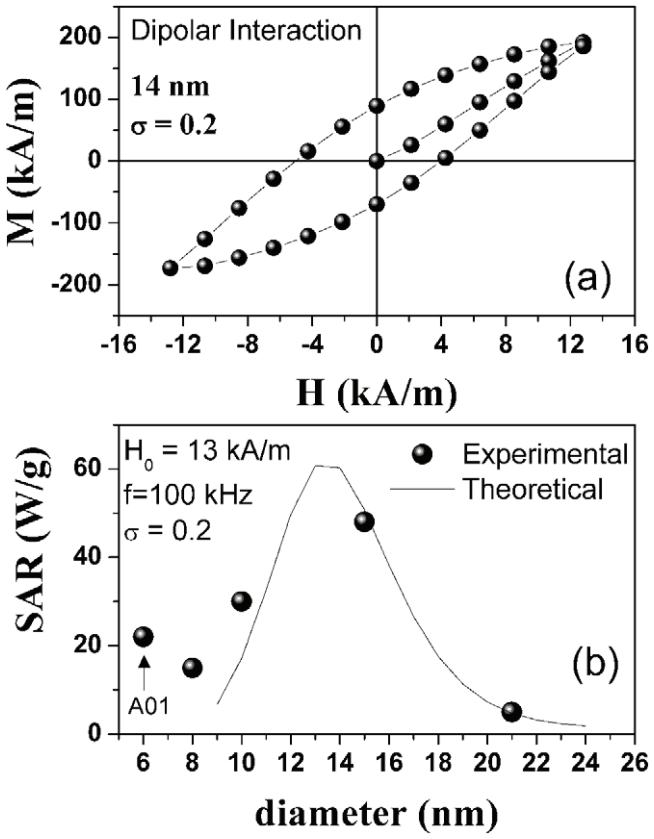

Figure 9. (a) Numerically calculated minor loops (up to $H = 13\,\text{kA m}^{-1}$ and at $T = 310$ K) of agglomerated (interacting) nanoparticles with a lognormal size distribution ($\langle d \rangle = 14$ nm and $\sigma = 0.2$) and random easy axis distribution. We also consider the values of $K_{\text{eff}} = 3 \times 10^4\,\text{J m}^{-3}$, $\tau_0 = 1 \times 10^{-11}$ s and $M_S = 500\,\text{kA m}^{-1}$. ($b$) Diameter dependence of the SAR of agglomerated and interacting nanoparticles (line), calculated from the area of the minor loops up to $13\,\text{kA m}^{-1}$ with $f = 100$ kHz. The solid symbols correspond to the experimental SAR measured for agglomerated samples A02–A05 with $f = 100$ kHz and $H_0 = 13\,\text{kA m}^{-1}$.

4. Discussion

According to the results pointed above on the hydrodynamic diameter and T_B of dispersed systems (samples DXX), it is expected that the Néel and Brown relaxation processes will contribute to the heat generation in the SAR experiments. Thus, the heat generation of dispersed samples should be described by the Rosensweig model [12]. According to this model, both relaxations take place in parallel and can be treated in an independent way. Thus, the effective relaxation time τ_{eff} is given by

$$\tau_{\text{eff}}^{-1} = \tau_B^{-1} + \tau_N^{-1}, \tag{10}$$

where τ_B and τ_N are the Brown and Néel relaxation times, respectively. Thus, the SAR of the system is determined by

$$\text{SAR} = \frac{\mu_0 H_0^2 2\pi f \chi_0 \tau_{\text{eff}}}{1 + (2\pi f \tau)^2}, \tag{11}$$

where χ_0 is the initial susceptibility of the system and the SAR presents a maximum at $2\pi f = \tau_{\text{eff}}^{-1}$. The dashed bars in figure 10(a) give the values of SAR as a function of $\langle d \rangle$ calculated with equation (11) for systems similar to our dispersed nanoparticles (ferrite nanoparticles with lognormal size distribution) under our SAR measurement conditions: $\sigma = 0.2$; $K_{\text{eff}} = 3 \times 10^4\,\text{J m}^{-3}$, $M_S = 400\,\text{kA m}^{-1}$, $\tau_0 = 1 \times 10^{-11}$ s, $\eta = 0.59 \times 10^{-3}$ Pa s (toluene), $f = 100$ kHz

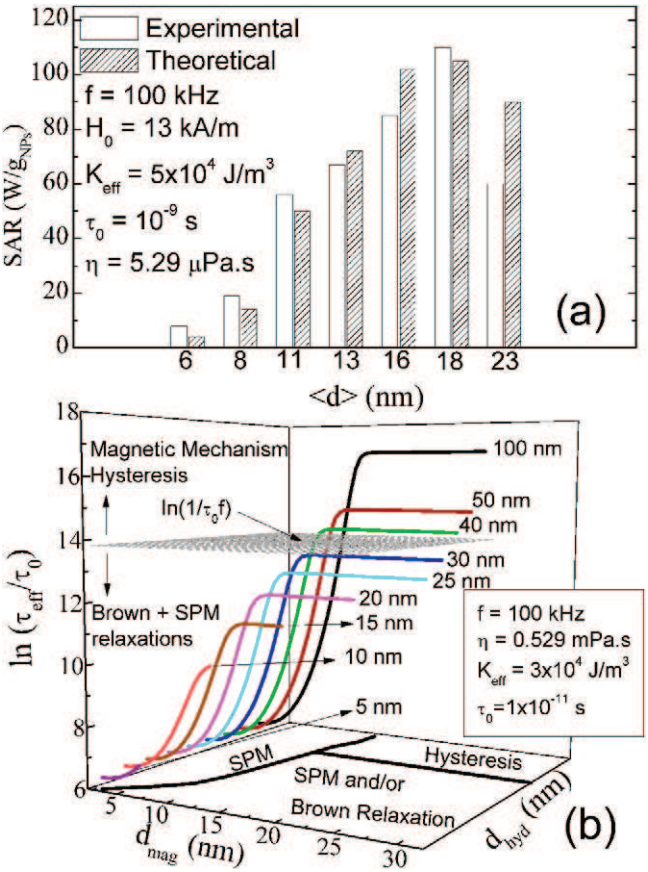

Figure 10. (*a*) Experimental and theoretical (calculated from equation (10)) values of SAR for dispersed samples taking the values of M_S, $\langle d \rangle$ and σ given in table 1 for each sample, and considering $f = 100\,\text{kHz}$, $H_0 = 13\,\text{kA m}^{-1}$, $K_{\text{eff}} = 3 \times 10^4\,\text{J m}^{-3}$ and $\tau_0 = 1 \times 10^{-11}\,\text{s}$. (*b*) Plot of the effective relaxation time τ_{eff} calculated from equation (9) as a function of the magnetic diameter d_{mag} and hydrodynamic diameter d_{hyd}. The gray plane indicates the value of $\ln(1/\tau_0 f)$. A diagram with the mechanisms involved in the heat generation for the values of d_{mag} and d_{hyd} is presented in the plane *xy*.

and $H_0 = 13\,\text{kA m}^{-1}$. We have also plotted the experimental values of SAR measured for samples DXX at 100 kHz and $13\,\text{kA m}^{-1}$ in figure 10(*a*). In fact, the predicted values are close to the experimental ones of the dispersed samples, indicating that the Rosensweig model (considering Néel and Brown relaxation times) can satisfactorily describe the heat generation of dispersed nanoparticles in our SAR experiments. An important feature to be considered is that the dispersed nanoparticles can be in the superparamagnetic regime for dc experiments (improves the biocompatibility), but in the blocked regime in the ac experiment, which can increase the SAR of the system for the working frequency in hyperthermia.

For our agglomerated nanoparticles (samples AYY), the large values of hydrodynamic diameter and the absence of superparamagnetic regime for $T > 300\,\text{K}$ even in dc measurements make the Néel and Brown relaxations be disregarded as heat generation mechanism under our SAR experimental conditions. Thus, for the agglomerated systems only the magnetic mechanism of dissipation in the blocked regime is present and the hysteresis area plays the fundamental role. The solid line in figure 9 gives the SAR values calculated as described in section 4 for systems similar to the agglomerated samples, taking into account interparticle interactions and considering a size dispersion of $\sigma = 0.2$. The simulated SAR values present similar behaviour to that of experimental data and both curves are relatively close.

According to our results, the Rosensweig model considering the Néel and Brown relaxations very well describes the SAR dependence of the dispersed samples on the mean diameter, while the SAR of agglomerated samples match with those calculated by our model described in section 4 considering the hysteresis area of the minor loop of interacting nanoparticles where H_0 is not negligible compared with the effective anisotropy field of the system.

The mechanisms involved in the SAR of a ferrofluid depend on the viscosity of the liquid, the anisotropy energy barrier, the hydrodynamic diameter (agglomeration must be considered), from the ac magnetic field amplitude and from the frequency of the experiment, i.e. from the comparison of $f = 100\,\text{kHz}$ with the relaxation times (for higher f, the hysteresis becomes important). Thus, similar nanoparticles can present different SARs resulting from distinct heating mechanisms depending on the rheological properties and the conditions of the SAR experiment, specifically the frequency, the field amplitude and the concentration of the nanoparticles. Each hyperthermia experiment should be analysed in these terms and experiments with similar nanoparticles may present distinct SAR for different concentrations and frequencies of the ac magnetic field.

Knowing the magnetic properties of a non-interacting nanoparticle system, the viscosity of the liquid and the hyperthermia experimental conditions (f, H_0), we can calculate a diagram of the heat generation mechanisms as a function of the magnetic diameter d_{mag} and hydrodynamic diameter d_{hyd}. In figure 10(*b*), we plot the effective relaxation times (τ_{eff}) as a function of the magnetic diameter d_{mag} and hydrodynamic diameter d_{hyd} calculated with the Rosensweig model for $f = 100\,\text{kHz}$ and $H_0 = 13\,\text{kA m}^{-1}$, considering $K_{\text{eff}} = 3 \times 10^4\,\text{J m}^{-3}$ and $\tau_0 = 10^{-11}\,\text{s}$. At a different experimental frequency, the influence zone of the Néel and Brown relaxations will change, being shifted to lower values of d_{hyd} and d_{mag} with increasing f. For our dispersed samples τ_N and τ_B are lower than $1/f$. Then, Néel and Brown relaxations dominate the heat generation. For agglomerated nanoparticles, the system is in the blocked regime and τ_B is far larger than $1/f$ ($10^{-5}\,\text{s}$), thus the hysteresis area of the minor loops determines the SAR of these systems. It is important to note that the diagram of the heat generation mechanism as a function of d_{mag} and d_{hyd} will be different for each system and SAR measurement conditions. Our diagram was built for $f = 100\,\text{kHz}$ and $H_0 = 13\,\text{kA m}^{-1}$, but a similar analysis can be made in order to interpret other results obtained under distinct experimental conditions, such as those observed in [21] and [42]. In these works, different contributions (superparamagnetism, Brown relaxation and hysteresis area) for heat generation were observed for nanoparticle systems, depending on the experimental conditions as well as on the magnetic and rheological properties.

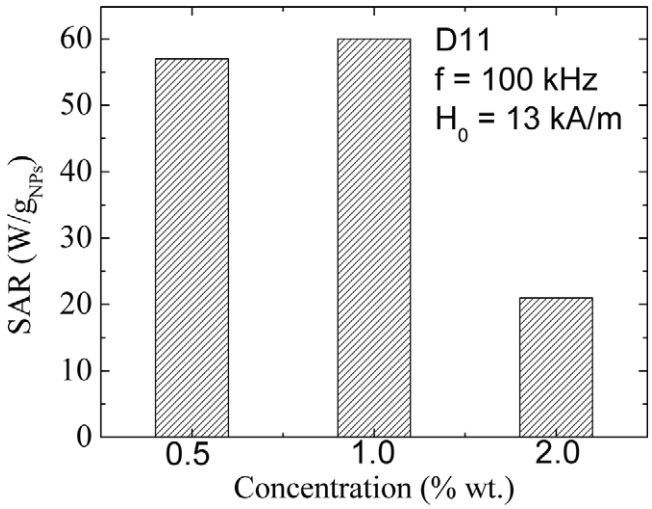

Figure 11. SAR values of sample D11 measured as a function of the concentration of the nanoparticles in the liquid measured with $f = 100\,\text{kHz}$ and $H_0 = 13\,\text{kA m}^{-1}$.

An interesting point to be discussed is the zone limiting the mechanisms. The Néel relaxation time has an exponential dependence on the volume, while the Brown relaxation time has a linear one, thus the region of d_{mag} and d_{hyd}, where both have similar values, is very narrow. On the other hand, the effects of Brown movement on the hysteresis area with changing d_{hyd}, lead to a broad frontier. The calculation of the hysteresis loops considering the Brown relaxation is not trivial and does not present an analytical solution [15]. It can be calculated numerically, but for a real system the interparticle interactions should be taken into account, which complicates the calculation.

We also measured the SAR as a function of the concentration of nanoparticles D11 in toluene for concentrations of 0.5, 1 and 2% w/w and the results are presented in figure 11. As observed, the value of SAR changes slightly from 0.5 to 1% w/w, while it is reduced more than 50% for 2% w/w. For the latter concentration, we observe a precipitation of the nanoparticles after 5 min, indicating that the nanoparticles are agglomerated. In fact, the SAR value obtained is close to that calculated with our model for agglomerated nanoparticles with a similar diameter distribution ($\sim$20 W g^{-1}). Thus, probably the heating mechanism changes from the two lower concentrations to the higher one: in the first case, the heating mechanism is based on the Néel and Brown relaxations, while for the concentration of 2 wt% the hysteresis area gives the SAR of the system. This experiment cannot be made for the agglomerated particles since they are still agglomerated even at low concentrations as a consequence of the synthesis procedure. In this way, the properties of the system would be independent of the concentration and the hysteresis areas would always determine the SAR value of the agglomerated system.

As pointed out by Carrey *et al* [15], the tuning of the magnetic characteristics in order to optimize the SAR of the nanoparticles is very interesting, since different results of magnetic measurements and microscopy images indicate that the nanoparticles are generally agglomerated in *in vitro* experiments after their absorption by the cells [10, 11]. In this way, the hydrodynamic radius of the nanoparticles would be increased, and the blocking temperature of the system resulting from the interparticle interactions and the hysteresis losses would determine the SAR of the system. Thus, our experimental and theoretical results presented here could be of interest for *in vitro* and *in vivo* hyperthermia experiments or even for future clinical applications.

5. Conclusions

We showed that intensely agglomerated 15 nm Fe_3O_4 nanoparticles with strong interparticle interactions present a moderate SAR as high as 48 W g^{-1} for an ac magnetic field with $f = 100\,\text{kHz}$ and $H_0 = 13\,\text{kA m}^{-1}$. According to our calculations and analyses, the heating capability of some of our systems (agglomerated and interacting nanoparticles) is a consequence of the hysteresis losses under optimal conditions ($\langle d \rangle = 15\,\text{nm}$). In our agglomerated systems, the hysteresis losses are a consequence of the frequency of the applied field used in the SAR measurement (100 kHz), added to the increment of the blocking temperature of the systems promoted by the interparticle interactions together with high value of the hydrodynamic diameter. The value of SAR observed on our agglomerated 15 nm nanoparticles could be increased with a narrower diameter dispersion of the particles. For comparison, we have also presented the SAR measurement as a function of the diameter for dispersed nanoparticles with a lower hydrodynamic diameter and a blocking temperature lower than 300 K, showing that for these systems the heat generation is produced by Néel and Brown relaxations.

Acknowledgments

The authors are grateful to Dr Monica Guraya and her research group at the Centro Atómico Bariloche, Argentina, for the Hydrodynamic Measurements. The authors also are grateful to the Materials Characterization Laboratory of Centro Atomico Bariloche for the use of the XRD diffractometer. M E Saleta and F B Effenberger thank the Argentinian and Brazilian agencies CONICET and CNPq, respectively, for PhD fellowships. This work was supported by the Argentinean agencies ANPCyT (PICT2007-832), CONICET (PIP2008-1333), UNCuyo grants, and by the Joint Project CAPES-MinCyT BR/08/24.

References

[1] Hilger I, Hiergeist R, Hergt R, Winnefeld K, Schubert H and Kaiser W A 2000 Thermal ablation of tumors using magnetic nanoparticles an *in vivo* feasibility study *Invest. Radiol.* **37** 580–6

[2] Kikumori T, Kobayashi T, Sawaki M and Imai T 2009 Anti-cancer effect of hyperthermia on breast cancer by magnetite nanoparticle-loaded anti-HER2 immunoliposomes *Breast Cancer Res. Treat.* **113** 435–41

[3] Hou C M, Hsueh Y S, Lin J, Wu H C and Lin F H 2009 The *in vivo* performance of biomagnetic hydroxyapatite nanoparticles in cancer hyperthermia therapy *Biomaterials* **30** 3956–60

[4] Maier-Hauff K *et al* 2007 Intracranial thermotherapy using magnetic nanoparticles combined with external beam radiotherapy: results of a feasibility study on patients with glioblastoma multiforme *J. Neurooncol.* **81** 53–60

[5] Ito A, Honda H and Kobayashi T 2006 Cancer immunotherapy based on intracellular hyperthermia using magnetite nanoparticles: a novel concept of 'heat-controlled necrosis' with heat shock protein expression *Cancer Immunol. Immunother.* **55** 320–8

[6] Berry C C and Curtis A S G 2003 Functionalisation of magnetic nanoparticles for applications in biomedicine *J. Phys. D: Appl. Phys.* **36** R198–206

[7] Goya G F, Lima E Jr, Arelaro A D, Torres T, Rechenberg H R, Rossi L M, Marquina C and Ibarra M R 2008 Magnetic hyperthermia with Fe_3O_4 nanoparticles: the influence of particle size on energy absorption *IEEE Trans. Magn.* **44** 4444–7

[8] Hergt R, Dutz S and Zeisberger M 2010 Validity limits of the Néel relaxation model of magnetic nanoparticles for hyperthermia *Nanotechnology* **21** 015706

[9] Bae S, Lee S W, Hirukawa A, Takemura Y, Jo Y H and Lee S G 2009 AC magnetic-field-induced heating and physical properties of ferrite nanoparticles for a hyperthermia agent in medicine *IEEE Trans. Nanotechnol.* **8** 86–93

[10] Fortin J-P, Gazeau F and Wilhelm C 2008 Intracellular heating of living cells through Néel relaxation of magnetic nanoparticles *Eur. Biophys. J.* **37** 223–8

[11] Marcos-Campos I, Asín L, Torres T E, Marquina C, Tres A, Ibarra M R and Goya G F 2011 Cell death induced by the application of alternating magnetic fields to nanoparticles-loaded dentritic cells *Nanotechnology* **22** 205101

[12] Rosensweig R E 2002 Heating magnetic fluid with alternating magnetic field *J. Magn. Magn. Mater.* **252** 370–4

[13] Landau L D and Lifshits E M 1960 *Electrodynamics of Continuous Media* (London: Pergamon)

[14] Usov N A 2010 Low frequency hysteresis loops of superparamagnetic nanoparticles with uniaxial anisotropy *J. Appl. Phys.* **107** 123909

[15] Carrey J, Mehdaoui B and Respaud M 2011 Simple models for dynamic hysteresis loop calculations of magnetic single domain nanoparticles: application to magnetic hyperthermia optimization *J. Appl. Phys.* **109** 083921

[16] El Mrabti H, Déjardin P M, Titov S V and Kalmykov Yu P 2012 Damping dependence in dynamic magnetic hysteresis of single-domain ferromagnetic particles *Phys. Rev.* B **85** 094425

[17] Zeng Q, Baker I, Loudis J A, Liao Y, Hoopes P J and Weave J B 2007 Fe/Fe oxide nanocomposite particles with large specific absorption rate for hyperthermia *Appl. Phys. Lett* **90** 233112

[18] Hergt R, Hiergeist R, Zeisberger M, Shüler D, Heyen U, Hilger I and Kaiser W 2005 Magnetic properties of bacterial magnetosomes as potential diagnostic and therapeutic tools *J. Magn. Magn. Mater.* **293** 80–6

[19] Hergt R, Dutz S and Zeisberger M 2010 Validity limits of the Néel relaxation model of magnetic nanoparticles for hyperthermia *Nanotechnology* **21** 015706

[20] Lima E Jr, Zysler R D, Goya G F, Torres T, Arelaro A D, Rechenberg H R, Marquina C and Ibarra M R 2008 Radio-frequency heat generation in magnetic nanoparticles: influence of particle size *FCM* 08—*At the Frontiers of Condensed Matter IV: Current Trends and Novel Materials (Buenos Aires, Argentina, 9–12 December 2008)*

[21] Noh S-h, Na W, Jang J-t, Lee J-H, Lee E J and Moon S H 2012 Nanoscale magnetism control via surface and exchange anisotropy for optimized ferrimagnetic hysteresis *Nano Lett.* **12** 3716–21

[22] Eggeman A S, Majetich S A, Farrel D and Pankhurst Q A 2007 Size and concentration effects on high frequency hysteresis of iron oxide nanoparticles *IEEE Trans. Magn.* **43** 2451–3

[23] Urtizberea A, Natividad E, Arizaga A, Castro M and Mediano A 2010 Specific absorption rate and Magnetic Properties of Ferrofluid with Interactions effects at low concentrations *J. Phys. Chem.* C **114** 4916–22

[24] Jeun M, Bae S, Tomitaka A, Takemura Y, Park K H, Paek S H and Chung K-W 2009 Effects of particle dipole interaction on the ac magnetically induced heating characteristics of ferrite nanoparticles for hyperthermia *Appl. Phys. Lett.* **95** 082501

[25] Dennis C L, Jackson A J, Borchers J A, Hoopes P J, Strawbridge R, Foreman A R, van Lierop J, Grüttner C and Ivakov R 2009 Nearly complete regression of tumors via collective behavior of magnetic nanoparticle in hyperthermia *Nanotechnology* **20** 395103

[26] Timko M *et al* 2009 Magnetic properties and heating effect in bacterial magnetic nanoparticles *J. Magn. Magn. Mater.* **321** 1521–4

[27] Hergt R, Dutz S and Röder M 2005 Effects of size distribution on hysteresis losses of magnetic nanoparticles for hyphertermia *J. Phys.: Condens. Matter.* **20** 385214

[28] Barbeta V B, Jardim R F, Kiyohara P K, Effenberger F B and Rossi L M 2010 Magnetic properties of Fe_3O_4 nanoparticles coated with oleic and dodecanoic acids *J. Appl. Phys.* **107** 073913

[29] Sun S and Zeng H 2002 Size-controlled synthesis of magnetite nanoparticles *J. Am. Chem. Soc.* **124** 8204–5

[30] Vargas M and Zysler R D 2005 Tailoring the size in colloidal iron oxide magnetic nanoparticles *Nanotechnology* **16** 1474–6

[31] Lima E Jr, De Biasi E, Vasquez Mansilla M, Saleta M E, Effenberg F, Rossi L M, Cohen R, Rechenberg H R and Zysler R D 2010 Surface effects in the magnetic properties of crystalline 3 nm ferrite nanoparticles chemically synthesized *J. Appl. Phys.* **108** 103919

[32] Zysler R D, Lima E Jr, Vasquez Mansilla M, Troiani H E, Mojica Pisciotti M L, Gurman P, Lamagna A and Colombo L 2013 A new quantitative method to determine the uptake of SPIONs in animal tissue and its application to determine the quantity of nanoparticles in the liver and lung of Balb-c mice exposed to the SPIONs *J. Biomed. Nanotechnol.* **9** 1–4

[33] Natividad E, Castro M and Mediano A 2009 Adiabatic vs. non-adiabatic determination of specific absorption rate of ferrofluids *J. Magn. Magn. Mater.* **321** 1497–500

[34] Vargas J M, Lima E Jr, Zysler R D, Duque J G S, De Biasi E and Knobel M 2008 Effective anisotropy field variation of magnetite nanoparticles with reduction *Eur. Phys. J.* B **64** 211–8

[35] Soon Gu Kwon and Taeghwan Hyeon 2011 Formation mechanism of uniform nanocrystals via hot-injection and heat-up methods *Small* **7** 2685–702

[36] Lima E Jr, Vargas J M, Rechenberg H R and Zysler R D 2008 Interparticle interactions effects on the magnetic order in surface of Fe_3O_4 nanoparticles *J. Nanosci. Nanotechnol.* **8** 5913

[37] De Biasi E, Zysler R D, Ramos C A and Knobel M 2008 A new model to describe the crossover from superparamagnetic to blocked magnetic nanoparticles *J. Magn. Magn. Mater.* **320** e312–5

[38] Châtel P F, Nándori I, Hakl J and Vad K 2009 Magnetic particle hyperthermia: Néel relaxation in magnetic

nanoparticles under circularly polarized field *J. Phys.: Condens. Matter.* **21** 124202
[39] Kashevsky B E, Agabekov V E, Kashevsky S B, Kekalo K A, Manina E Yu, Prokhorov I V and Ulashchik V S 2008 Study of cobalt ferrite nanosuspensions for low-frequency ferromagnetic hyperthermia *Particuology* **6** 322–33
[40] Dorman J L and Fiorani D (ed) 1992 *Magnetic Properties of Fine Particles* (Amsterdam: North Holland)
[41] Garcia-Otero J, Garcia-Bastida A J and Rivas J 1998 Influence of temperature on the coercive field of non-interacting fine magnetic particles *J. Magn. Magn. Mater.* **189** 377
[42] Bakoglidis K D, Simeonidis K, Sakellari D, Stefanou G and Angelakeris M 2012 Size-dependent mechanisms in ac magnetic hyperthermia response of iron-oxide nanoparticles *IEEE Trans. Magn.* **48** 1320–3